Polymer Composites

WILEY | spe INSPIRING PLASTICS PROFESSIONALS

RESEARCH ARTICLE

Flexural Properties of 3D Braided Jute/Epoxy Composite Honeycombs: Structure–Property Relationships

Qianqian Li[1,2,3] | René Alderliesten[4] | Honghua Zhang[5] | Yan Zhang[5] | Hui Zhang[1,3] | Wei Li[3,5] | Jianyong Yu[2] | Yasmine Mosleh[6]

[1]College of Materials Science and Engineering, State Key Laboratory for Modification of Chemical Fibers and Polymer Materials, Donghua University, Shanghai, China | [2]Innovation Center for Textile Science and Technology, Donghua University, Shanghai, China | [3]Center for Civil Aviation Composites, Shanghai High Performance Fibers and Composites Center, Donghua University, Shanghai, China | [4]Aerospace Structures and Materials, Faculty of Aerospace Engineering, Delft University of Technology, Delft, the Netherlands | [5]College of Textiles, Donghua University, Shanghai, China | [6]Biobased Structure and Materials, Faculty of Civil Engineering and Geosciences, Delft University of Technology, Delft, the Netherlands

Correspondence: Wei Li (liwei@dhu.edu.cn) | Jianyong Yu (yujy@dhu.edu.cn)

Received: 15 September 2025 | **Revised:** 28 October 2025 | **Accepted:** 9 December 2025

Keywords: 3D braid | flexural stiffness | honeycomb structure | natural fiber | structure–property relationship

ABSTRACT

An integrated molding composite honeycomb has been proposed, in which a seamless, 3D braided natural fiber cellular fabric serves as the reinforcement, with epoxy resin as the matrix. Three-point bending behaviors of the honeycomb, taking account of the effects of joint wall length and opening angle, were investigated. The fracture mechanisms during bending were monitored using 3D Digital Image Correlation. The validated Finite element model was developed and used to perform a parametric analysis identifying the effect of material Young's modulus and geometric variations on the flexural stiffness. The results reveal that fracture occurs at the junction of the joint wall and the free wall, characterized by shear-type failure and structural geometry parameters significantly affect flexural performance. Decreasing the joint wall length from 55 to 4 mm in 90° honeycombs reduced the maximum load by approximately 26% and the flexural stiffness (P/y) by about 55%, accompanied by an increase in maximum deflection. Conversely, for specimens with a 17 mm joint wall, increasing the opening angle from 60° to 120° decreased the maximum load and P/y by approximately 32% and 55%, respectively, while the flexural deflection gradually increased. The knowledge generated from this study is key in design and performance evaluation of 3D braided composite honeycomb cores for sandwich structures, which is crucial for enhancing the out-of-plane bending resistance of sandwich structures.

1 | Introduction

Honeycomb sandwich structures are widely employed across diverse sectors [1–3], from the aerospace to rail transport [4], owing to their superior specific mechanical properties [5] and multifunctional integration capabilities (e.g., sound absorption [6–9], thermal insulation [7, 10], and electromagnetic shielding [11, 12]). Tailoring the honeycomb core architecture provides a more convenient route to enhance mechanical performance than altering the constituent materials or panel geometry [13, 14]. The growing demand for low-weight, high-performance sandwich cores has spurred interest in fiber-reinforced polymer honeycombs [15, 16]. While synthetic fibers like carbon and glass enhance composite properties, their high cost and environmental impact have driven the search for sustainable alternatives, such as natural fibers and wood composites [17]. Among them, jute stands out as a compelling choice for sustainable structural composites due to its clear environmental and economic benefits. Concurrently, 3D braided technology offers significant benefits over traditional laminates, including improved

damage tolerance and through-thickness reinforcement, driven by its near-net-shape manufacturability and excellent mechanical performance [18, 19].

Consequently, the development of a 3D braided jute/epoxy honeycomb represents a strategic merge of the sustainability and low cost of a natural fiber with a high-performance, integrated structural design. This makes it a highly relevant candidate for applications where weight, cost, and environmental impact are critical, such as in transportation, vehicle interiors, and sustainable infrastructure [20]. The fundamental principle of braiding and the in-plane compression behavior of such structures has been comprehensively examined in our previous research efforts [20, 21].

Bending behavior is a pivotal consideration for sandwich structures in practical applications like floor panels in aircraft and vehicles, where they must withstand bending moments and shear stresses [5, 22]. Therefore, a thorough investigation of the bending properties of 3D braided composite honeycombs is essential for refining their design and ensuring they meet application requirements. Assessing the flexural deformation of honeycombs is non-trivial, as equivalent elastic moduli from in-plane deformation often fail to capture the flexural response due to distinct moment distributions in the cell walls [23, 24]. While previous studies have developed analytical and numerical methods to evaluate the flexural stiffness of honeycomb cores [15, 23, 25], a significant research gap remains. Specifically, a systematic exploration of the combination of natural fibers and 3D braiding within a honeycomb core under bending loads is lacking. Existing research on natural fiber honeycombs has predominantly focused on 2D architectures, lacking the through-thickness reinforcement of 3D braiding [15, 17]. Conversely, studies on 3D braided composites have largely utilized synthetic fibers and concentrate on solid sections, rather than the specific geometric parameter sensitivity of a cellular honeycomb in flexure. Furthermore, the coupled effect of key geometric parameters (e.g., joint wall length and opening angle) on the failure mechanisms and flexural stiffness of an integrated, seamless 3D braided natural fiber honeycomb remains unquantified.

This study aims to address this gap by: (1) developing a seamless 3D braided jute/epoxy honeycomb core; and (2) systematically quantifying the individual and interactive effects of the joint wall length and opening angle on flexural performance, failure initiation, and damage progression. This investigation is conducted through three-point bending tests, complemented by digital image correlation (DIC) for full-field strain measurement. Additionally, an effective finite element analysis (FEA) model, employing necessary simplifications to balance computational cost and accuracy, is utilized to further study the influence of material and geometrical parameters on flexural stiffness.

2 | Materials and Methods

To isolate the effects of key geometric parameters on the flexural performance of 3D braided composite honeycombs, the control variable method was employed. The joint wall length and opening angle were specifically selected for experimental investigation. Isolating the joint wall length variation ensured a constant specimen width, which clarifies its individual effect on flexural behavior. In contrast, varying the free wall length or wall thickness would concurrently alter the specimen's width and length, thereby introducing confounding variables. The opening angle was chosen as it is a fundamental parameter defining cell geometry, known to critically influence mechanical properties and stress distribution [26, 27]. The selected range (60°, 90°, 120°) enables the examination of deformation and failure mode transitions from acute to obtuse geometries. Additionally, the opening angle is solely mold-dependent, guaranteeing consistency in the braiding process across all specimens.

2.1 | Sample Description

2.1.1 | Materials

The yarn used for braiding is jute yarn with an average diameter of 2 mm (double strands), purchased from http://jd.d.com. The matrix is provided by Shangwei (Tianjin) Wind Power Materials Company Limited. The mass ratio of the matrix to the curing agent is 100:30. The mechanical properties of the epoxy resin used are presented in Table 1.

It is noteworthy that the jute fibers were used as-received without any chemical pre-treatment, as the primary focus of this study is on the effect of geometric and structural parameters on the macroscopic flexural performance. Future work will delve into the optimization of fiber-matrix adhesion and its consequent effects on the mechanical properties.

2.1.2 | Braiding Procedure

3D braided honeycomb fabrics were fabricated using jute yarns on a self-made 3D braiding machine. A schematic of the custom braiding machine setup is depicted in Figure 1a. Employing the "four-step" method of 3D braiding (Figure 1d), the interweaving of the yarns can be adjusted by controlling movement of the yarn carrier. This allows for the manipulation of the fabric's integration (Figure 1e) and separation (Figure 1f), resulting in a 3D braided honeycomb fabric. Subsequently, the resultant fabric was employed to manufacture composite honeycomb via the Vacuum-Assisted Resin Transfer Molding (VARTM) process [20]. In the VARTM process, the dry 3D braided jute preform was placed in a mold, and the epoxy resin mixture was infused under vacuum to ensure thorough impregnation of the fibrous architecture. The setup was then cured under the conditions specified in Table 1. An exhaustive account of the fabrication methodology for the 3D braided honeycomb fabric and its composite has been documented in our earlier publication [20, 21], and the entire preparation process is illustrated in Figure 2a. To ensure statistical significance, each experimental group ($n = 5$) contained replicate specimens fabricated under identical processing conditions.

TABLE 1 | Parameters of the epoxy resin.

Density of two-component epoxy system						
SWANCOR 2511-1A	SWANCOR 2511-1BS	Tensile strength (MPa)	Tensile modulus (MPa)	Extensibility (%)	Flexural strength (MPa)	Flexural modulus (MPa)
1.1–1.2	0.9–1.0	67–80	2700–3500	4.5–8.5	110–140	2800–3600
Curing conditions: room temperature (28°C) 24 h + 8 h at 70°C.						

2.1.3 | Sample Encoding Description

A large number of samples were designed in this study. To facilitate description and differentiation, the samples were named as follows: [(Honeycomb Opening Angle: 60°, 90°, or 120°) – (Number of Complete Cell Columns along the *Y*-Axis: 2, 4, or 6)], as shown in Figure 2b.

The specific values for the joint wall length (corresponding to 2, 4, and 6 cell columns, resulting in lengths of approximately 4, 17, and 55 mm, respectively) were chosen primarily to ensure that all specimens contained an integer number of complete unit cells and were manufactured with the same number of braiding cycles, thereby maintaining consistency in the fabrication process. This range of lengths was also intentionally selected to cover a sufficiently wide spectrum, from very short joints to substantially long ones. This design allows for the observation of potential transitions in the dominant failure mechanism, such as from local cell wall bending to global buckling, providing comprehensive insight into the structure–property relationships.

The 3D braided honeycomb fabric has a controlled braiding angle of 32° and a pitch length of 6.7 mm. Each sample contains a total of 48 braiding cycles, with 2 cycles for the free wall. Due to the different number of braiding cycles applied to the joint walls, the number of cells in the fabric will vary accordingly. The specific number of braiding cycles for each sample set is outlined in Table S1. A comprehensive listing of the geometrical parameters for the samples is provided in Table S2.

2.2 | Description of Experiments

The flexural testing of the composite honeycombs was carried out using an MTS hydraulic universal testing machine (Model E45) with a maximum load capacity of 600 KN. During the test, each specimen was positioned on two rigid supports, and a loading nose applied a quasi-static vertical compressive force at a constant displacement rate of 2 mm/min [28]. Both the loading nose and the supports featured a radius of 9 mm. Concurrently, a 3D digital image correlation (3D-DIC) measurement system supplied by Correlated Solutions was employed to accurately quantify the deformation behavior of the 3D braided composite honeycomb under bending loads. The configuration of the experimental apparatus is illustrated in Figure 3. As stated in Section 2.1.2, five replicate specimens ($n = 5$) were tested for each experimental group. The key mechanical properties, including the maximum flexural load, maximum deflection, and the slope (P/y) of the initial linear portion of the load–displacement curve, are reported as the mean ± standard deviation (SD) in this study.

3 | Experimental Results and Discussion

3.1 | Flexural Curves and Failure Process

The flexural curves of 3D braided composite honeycombs with varying joint wall lengths and opening angles under flexural loads are shown in Figure 4a,b, respectively.

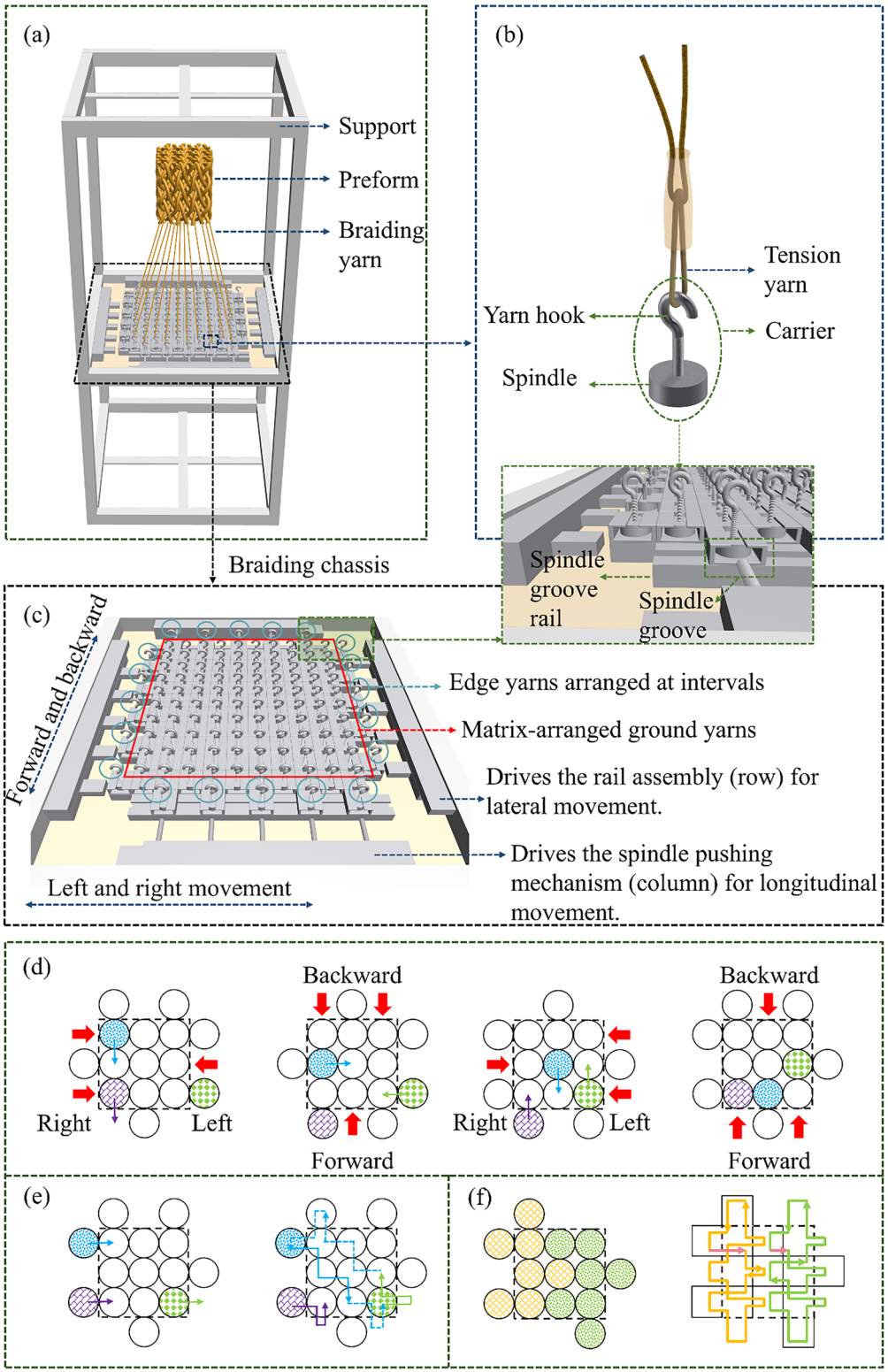

FIGURE 1 | (a) Schematic diagram of a track and column (Cartesian) 3D braiding machine (b) tension yarn and yarn carrier (c) braiding chassis (d) yarn carrier movement of the 3D braiding "four-step 1×1" method (e) yarn movement trajectory of the fabric's integration (f) yarn movement trajectory of the fabric's separation.

By selecting representative samples for detailed analysis, the curves can be divided into three distinct stages: OA, AB, and BC. In the OA stage, the curve shows a linear increase, indicating that the specimen is in the linear elastic deformation phase without any damage. During the AB stage, the curve represents a nonlinear increase as the load increases with the displacement, resulting in increased flexural deformation and a gradual decrease in flexural stiffness. The BC stage is characterized by a descending curve, where the load reaches the specimen's ultimate load-bearing capacity, ultimately leading to failure.

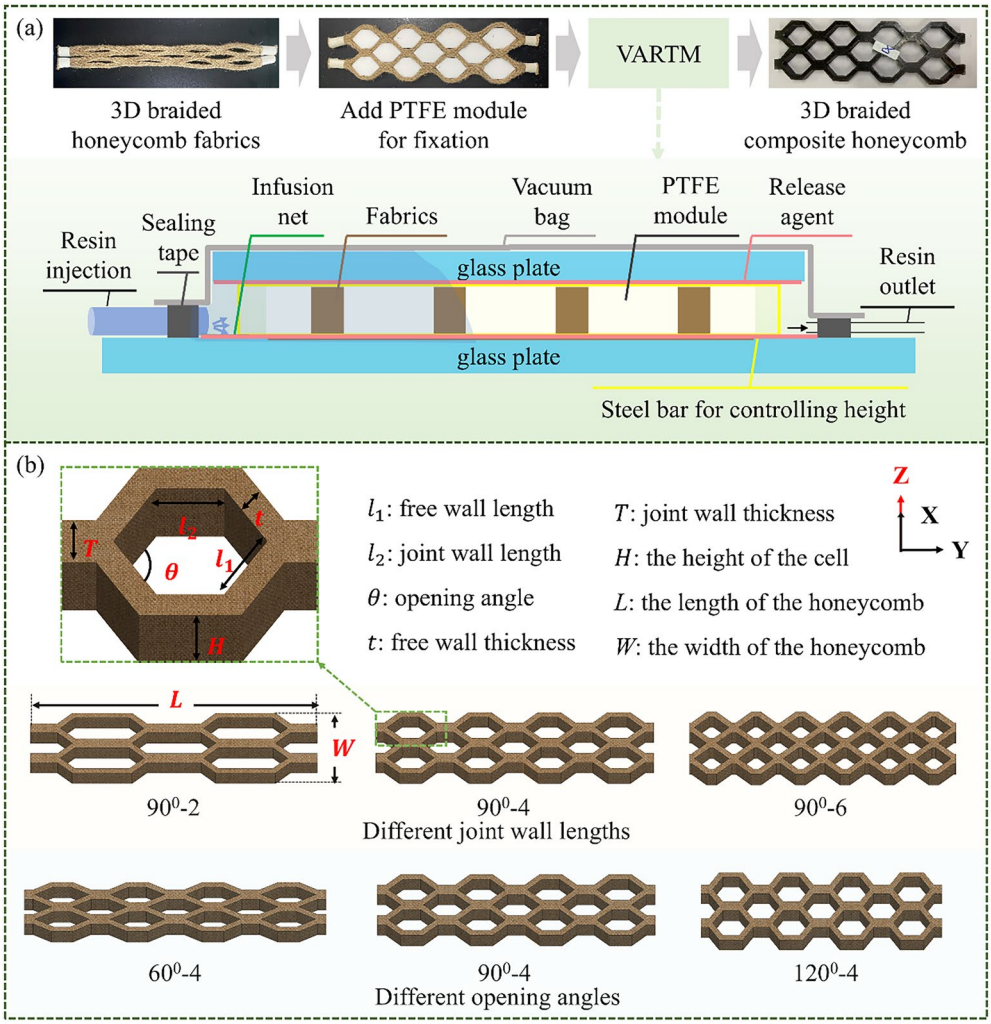

FIGURE 2 | The 3D braided composite honeycomb: (a) preparation process (b) samples and their parameters.

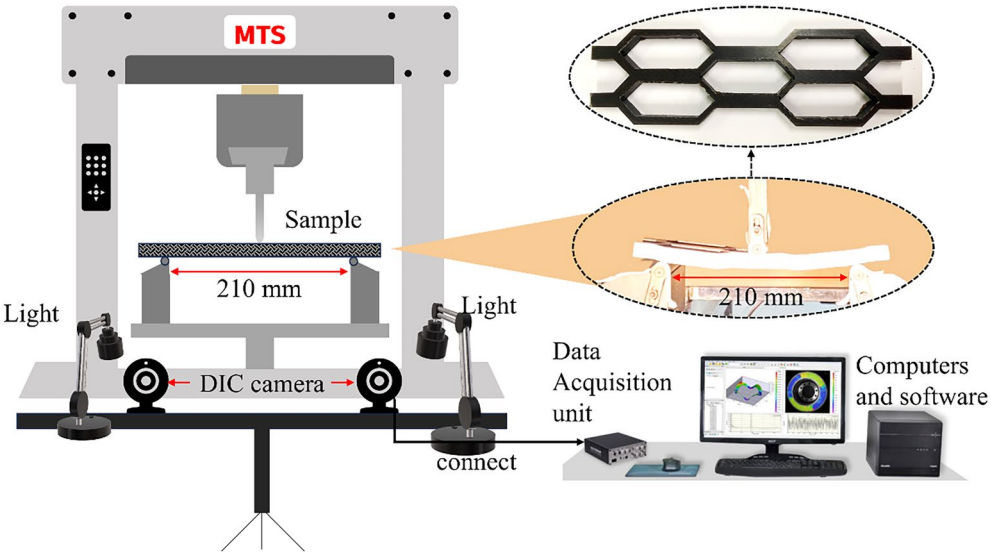

FIGURE 3 | The experimental apparatus.

The deflection-load curves for all the tested samples exhibited a "cliff-like" drop, indicating failure due to brittle fracture. Further analysis reveals that near the maximum load, some curves, such as that of the 90°-6 sample, exhibit a "sawtooth" pattern (viscoelastic behavior), while others, like the 90°-2 and 90°-4 samples, show a smooth, nonlinear gradual rise, reflecting

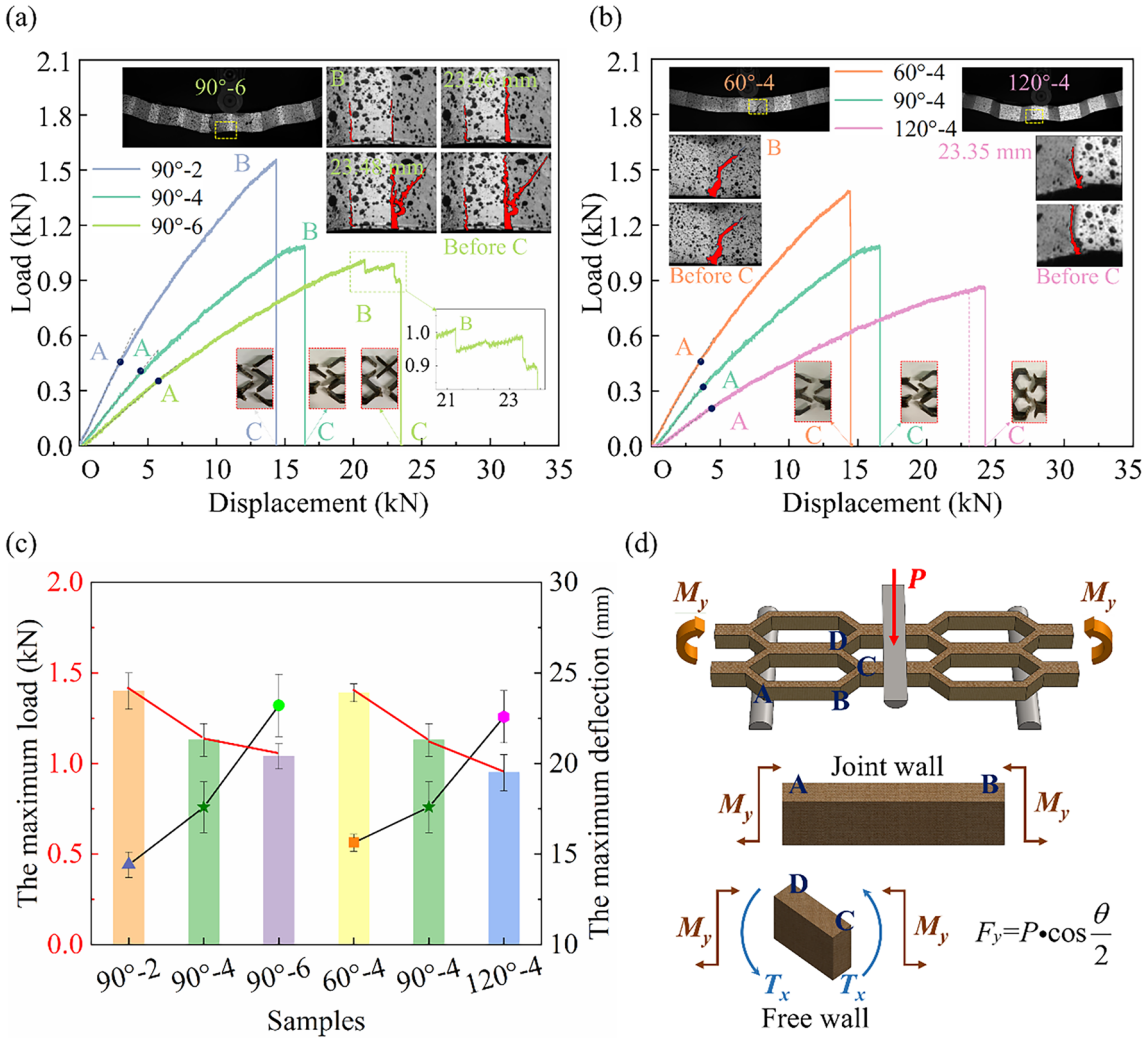

FIGURE 4 | Load–displacement curves for typical specimens with varying (a) joint wall lengths and (b) opening angles; (c) the maximum load and the maximum deflection of 3D braided composite honeycombs under flexural load; (d) simplified force diagram of the 3D braided composite honeycombs under flexural load.

their respective failure processes. The failure processes of 3D braided composite honeycombs with varying joint wall lengths and opening angles can be categorized into two types: (I) minor cracks develop before specimen failure, not affecting load-carrying capacity, leading to curves with nonlinear increases; (II) cracks develop and gradually propagate before specimen failure, resulting in "sawtooth-like" fluctuations near the maximum load.

3.2 | Flexural Properties of Composite Honeycombs

In 3D braided composite honeycombs, reducing the joint wall length or increasing the opening angle leads to a decrease in maximum flexural load and an increase in maximum deflection, as illustrated in Figure 4c. For specimens with a 90° opening angle, decreasing the joint wall length from 55 to 4 mm reduced the maximum load by ~26% (from ~1.40 to ~1.03 kN) and increased the maximum deflection by ~61% (from ~14.41 to ~23.21 mm). On the other hand, for specimens with a consistent joint wall length of 17 mm, increasing the opening angle from 60° to 120° reduced the maximum load by ~32% (from ~1.39 to ~0.95 kN) and increased the deflection by ~44% (from ~15.63 to ~22.58 mm).

Chen [23] demonstrated that during the flexural deformation of honeycomb structures, inclined cell walls generate flexural moments to maintain the angular configuration at the junctions. This behavior can be analyzed by modeling the cell walls as beams with fixed supports at both ends. Within this model, the joint wall primarily bears the bending moment (M_y), while the free wall is subjected to both the bending moment and torque (T_x), resulting in lower bending efficiency compared to the joint wall. From an energy-based perspective, the work done by the applied load is stored as strain energy, predominantly in the form of bending energy within these cell walls. A reduction in joint wall length diminishes the volume of material effectively participating in this elastic energy storage, leading to a lower overall structural stiffness and maximum load capacity. Similarly, an increase in the opening angle reduces the vertical component of the force resisting bending (F_y in Figure 4d), effectively weakening the structure's moment-resisting mechanism and resulting in higher compliance.

This mechanical response is consistent with analytical models for cellular solids, which often treat honeycombs as homogeneous orthotropic materials [29]. Accordingly, the structure can be equivalently treated as a rectangular beam, and its flexural stiffness D can be evaluated using the three-point bending formula (Formula 1) [30].

$$D = EI = E \cdot \frac{bh^3}{12} = \frac{l^3}{48} \cdot \frac{P}{y} \tag{1}$$

where D is the flexural stiffness (N·mm); E is the Young's modulus of the material (MPa), and I is the second moment of area of the cross-section (mm^4). For a beam of width b (mm) and height h (mm), $I = b \times h^3/12$. In the equation, l is the support span (mm), P is the applied load (N), and y is the deflection at the midspan (mm).

TABLE 2 | The P/y of 3D braided composite honeycombs.

Variable		Sample	$\frac{P}{y}$ ±SD (N/mm)
Joint wall length	55 mm	90°-**2**	146.09 ± 11.09
	17 mm	90°-**4**	90.64 ± 10.26
	4 mm	90°-**6**	65.58 ± 5.62
Opening angle	**60°**	**60°**-4	141.72 ± 9.00
	90°	**90°**-4	90.64 ± 10.26
	120°	**120°**-4	64.46 ± 10.01

This formula indicates that, for a constant support span l, the flexural stiffness D is proportional to the slope (P/y) of the initial segment of the load–displacement curve. Therefore, this study adopts P/y as a direct experimental parameter for comparing the flexural stiffness of the different honeycomb structures. The experimental values of P/y are presented in Table 2 as mean ± SD ($n = 5$).

The data in Table 2 shows that P/y follows the order 90°-2 > 90°-4 > 90°-6 for joint wall length and 60°-4 > 90°-4 > 120°-4 for opening angle. These observed trends—decreasing P/y with decreasing joint wall length or increasing opening angle—align qualitatively with the predictions of these models [29, 30], where the equivalent elastic modulus is a strong function of the relative density and cell wall orientation. This correlation confirms that the fundamental mechanics of our 3D braided composite honeycombs are governed by the same principles as conventional honeycombs, despite the integral nature of the braided architecture.

3.3 | Damage Analysis

Under flexural loads, the failure of 3D braided composite honeycombs initiates at the intersection of the joint wall and the free wall, as depicted in Figure 5. Fracture occurs asymmetrically, typically on one side rather than simultaneously on both sides of the pressure head. The fracture location can manifest in two scenarios: (I) direct fracture at the intersection of the free wall and the joint wall, indicated by the yellow arrows in Figure 5; (II) failure begins at the intersection and progressively extends toward the free wall, with cracks exhibiting an oblique pattern.

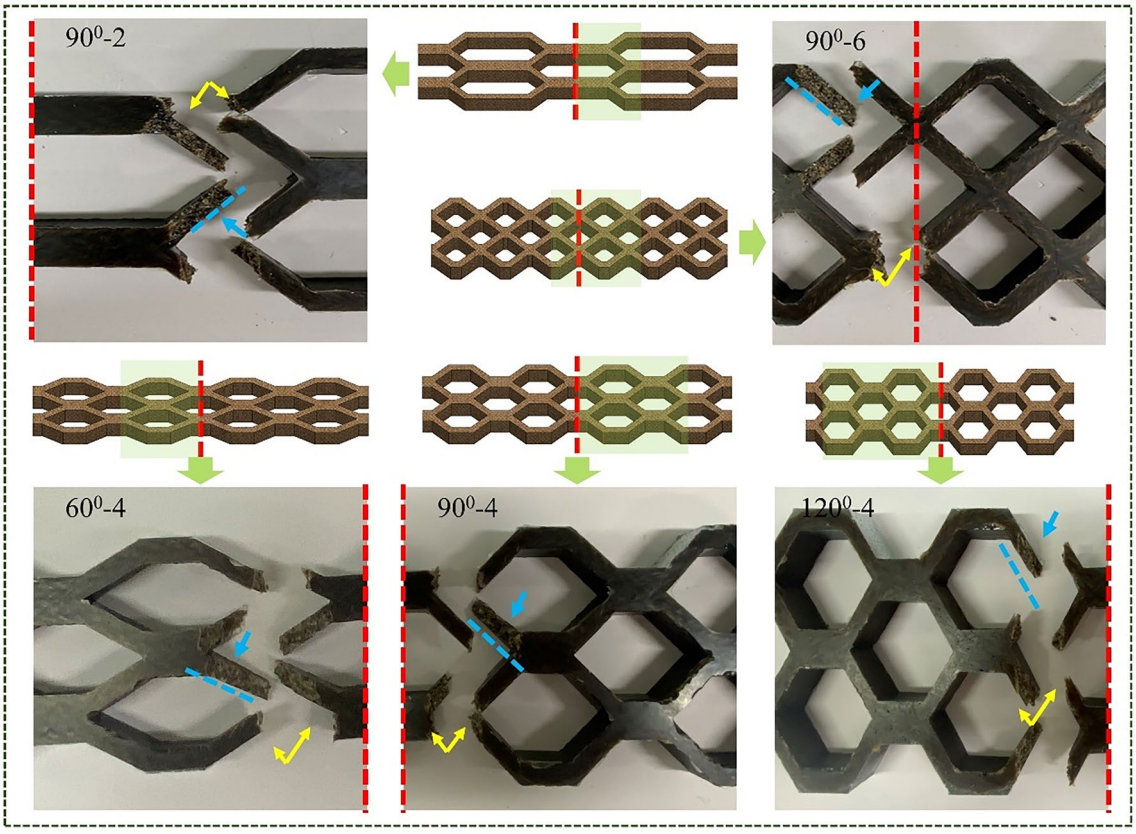

FIGURE 5 | Failure location of 3D braided composite honeycombs under flexural load.

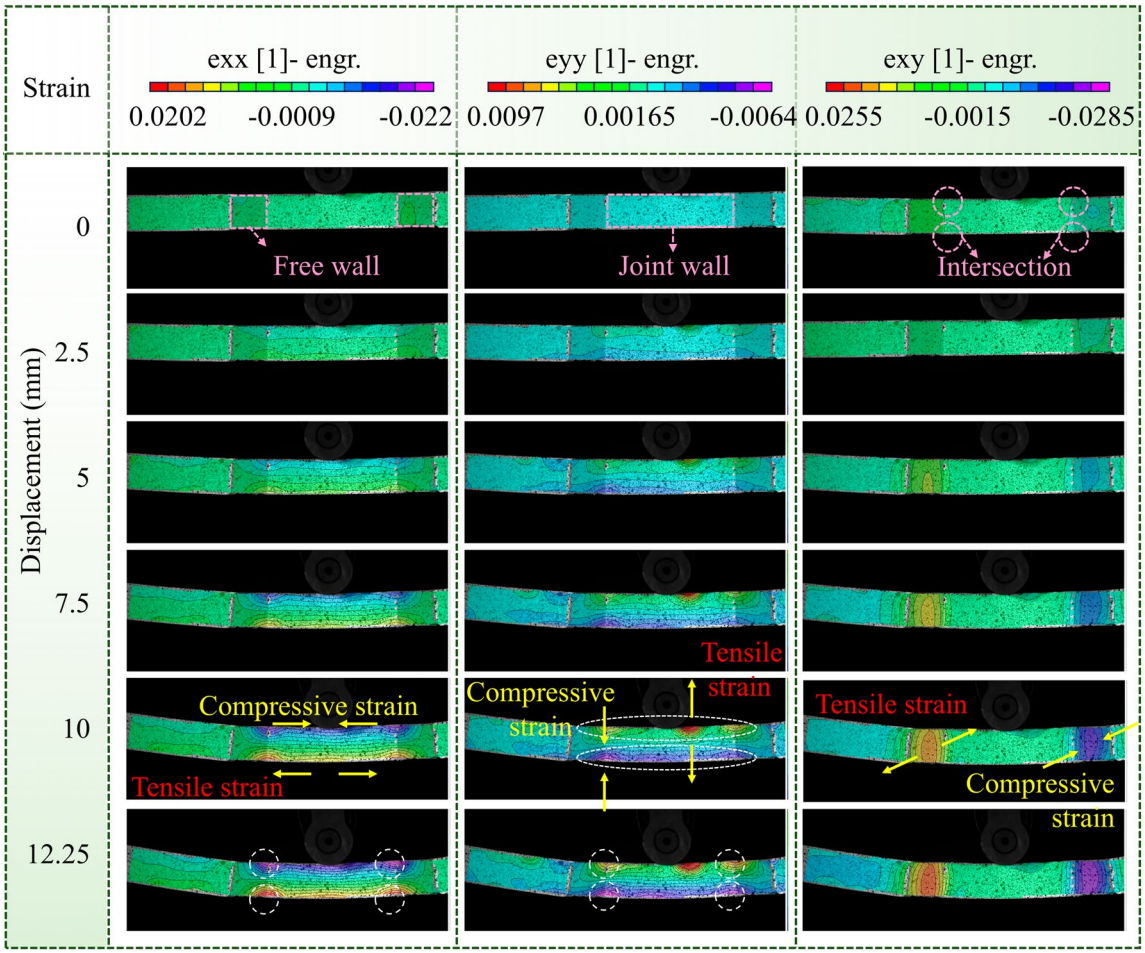

FIGURE 6 | Images captured by DIC during tests illustrating the strain changes as displacement increases under flexural loading (exx-lateral strain; eyy-longitudinal strain; exy-shear strain).

This results in a "shear-type" failure mode, as shown by the blue dashed line in Figure 5.

Analysis of the fracture section of the sample reveals that the fracture mode of 3D braided composite honeycombs under bending load is the same as that under in-plane compressive load. In both cases, yarn breakage, fiber breakage, matrix fracture, and fiber–matrix debonding can be observed [21]. Additionally, fractured yarn bundles and fractured fiber bundles distributed in four different directions are visible [21, 31]. It can thus be concluded that the fracture mode of 3D braided composite honeycombs under bending load belongs to the typical failure mechanism of fiber-reinforced composites.

3D-DIC was used to record the strain of 3D braided composite honeycombs under flexural loads, allowing for a detailed analysis of damage progression and failure modes. The strain under flexural loads for 90°-2 is depicted in Figure 6. According to the exx strain map, transverse strains initially emerge on the joint wall, gradually concentrating at the intersection of the free wall and the joint wall as displacement increases. The surface of the joint wall in contact with the loading nose experiences transverse compressive strain, while the underside experiences transverse tensile strain, with the most pronounced strains occurring at the intersection. From the eyy strain map, longitudinal strains are observed, showing that the surfaces of the joint wall in contact with the loading nose experience longitudinal tensile strain on both sides, while the underside experiences longitudinal compressive strain. Again, higher strains are noted at the intersection of the free wall and joint wall. Both exx and eyy strains concentrate at the "Y-shaped" junction, indicating a stress concentration point where the specimen is more susceptible to fracture. Exy strains appear solely on the free wall, with each side of the joint wall exhibiting inclined compressive and tensile shear strains in different directions. The strain distribution characteristics for samples 90°-4, 90°-6, 60°-4, and 120°-4 are similar to those of 90°-2.

Based on the analysis above, it is evident that under flexural loads, strain in 3D braided composite honeycombs concentrates at the "Y-shaped" junction where the free wall intersects with the joint wall. The free wall exhibits shear strain, leading to cracks initiating from this junction and presenting an inclined fracture surface on the free wall. On each side of the same joint wall, the free wall experiences shear strains in opposite directions—specifically inclined tensile and compressive strains. This effect arises because the joint wall bears greater load capacity than the free wall, causing stress to concentrate at the "Y-shaped" junction. If the free wall at this junction exhibits downward longitudinal and leftward transverse movement, resulting in inclined tensile strain, the right-side joint wall will similarly experience downward longitudinal and rightward transverse movement, forcing the connected

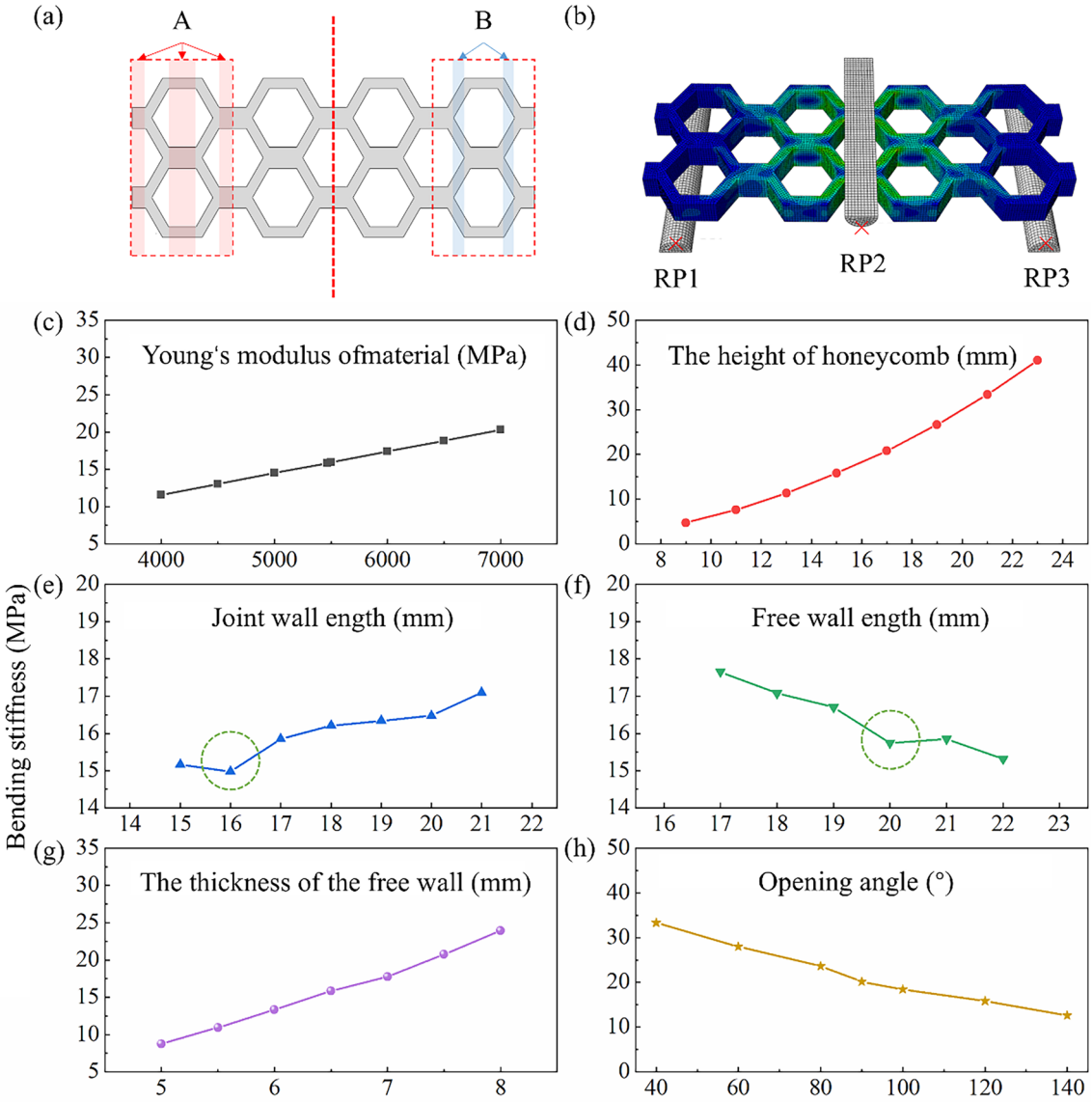

FIGURE 7 | (a) Schematic diagram of the contact position between the support fixture and the specimen (b) Finite element model of 120°-4; The influence of (c) material properties and (d–h) structural parameters on flexural stiffness.

right-side free wall to move upward and to the right, thus exhibiting inclined compressive strain. Consequently, the strains on the free walls at both ends of the joint wall differ, explaining why fractures occur only on one side of the pressure head rather than simultaneously on both sides.

4 | Exploring Flexural Stiffness of 3D Braided Composite Honeycombs Using FEA

As the length of the joint wall (l_2) increases, if the contact position between the support fixture and the specimen is located within area A (the joint wall) in Figure 7a, the area of the specimen in the span (l) remains unchanged. However, if the contact position is outside of area A or if the location of the contact changes (entering or exiting area A), the area of the specimen in the span (l) gradually decreases. Similarly, as the length of the free wall (l_1) increases, if the contact position between the support fixture and the specimen is within area B (the free wall) in Figure 7a, the area of the specimen in the span (l) remains constant. If the contact position moves outside area B or changes (entering or exiting area B), the area of the specimen in the span gradually increases. Additionally, as the wall thickness (t or T) increases, the area of the specimen in the span (l) gradually increases. The area of the specimen in the span (l) also gradually increases with an increase in the opening angle (θ).

This indicates that the flexural stiffness of 3D braided composite honeycomb is not solely dependent on the amount of material (the area of the specimen) within the span but is significantly influenced by its geometric shape. Therefore, it is essential to investigate the influence of variables, particularly geometric shape, on flexural stiffness using FEA [30].

4.1 | Geometry Creation and Description of FEA Model

Establishing a realistic model that precisely matches the 3D braided composite honeycomb is highly complex. Zhang et al.

TABLE 3 | Parameters of model 120°-4.

Sample	l_1 (mm)	l_2 (mm)	t (mm)	θ (°)	H (mm)	Support span (mm)
120°-4	21	17	6.5	120	15	210

TABLE 4 | Mesh convergence study for model 120°-4.

Mesh size (mm)	Number of elements	Simulated $\frac{P}{y}$ (N/mm)	Change vs. 1 mm (%)
1	151,725	83.93	Baseline
1.5	45,150	82.13	−2.14%
2	19,872	71.47	−14.84%
2.5	9732	74.17	−11.61%
3	5890	Failed to produce a convergent solution	

TABLE 5 | Comparison between experimental and simulated values of P/y.

Sample	Experimental values ± SD (N/mm)	Simulated values (N/mm)	Error (%)
90°-2	146.09 ± 11.09	158.43	7.79
90°-4	90.64 ± 10.26	104.53	13.29
90°-6	65.58 ± 5.62	82.52	20.53
60°-4	141.72 ± 9.00	148.92	4.84
120°-4	64.46 ± 10.01	82.13	21.52

[32] indicated that the computational results of homogenized models correspond well with their full-scale counterparts. Therefore, this section develops a homogenized model of 3D braided composite honeycombs to explore the factors influencing their flexural resistance. Based on the geometric parameters of the honeycombs, a homogenized equivalent solid model is created using SOLIDWORKS 2021 software and then imported into Abaqus software for analysis.

The boundary conditions were applied as follows: reference points RP1 and RP3 were fully fixed, while RP2 was assigned a displacement-controlled boundary condition to simulate the loading nose. The interaction between the support fixtures and the specimen was modeled as frictionless hard contact. The material was modeled as linear elastic and isotropic, with properties derived from experimental tensile tests on 3D braided jute/epoxy composites (Young's modulus = 5468.87 MPa, Poisson's ratio = 0.48), as shown in Figure S1 and Table S3. The finite element model of the 120°-4 configuration is illustrated in Figure 7b, with its parameters detailed in Table 3.

4.2 | Mesh Sensitivity and Convergence Analysis

A mesh sensitivity analysis was conducted to ensure the convergence and accuracy of the finite element results. The model 120°-4 was used for this analysis. The approximate global mesh size was varied from 1 to 3 mm. The flexural stiffness (P/y) was computed for each mesh size, with the results summarized in Table 4.

The results exhibit a non-monotonic convergence behavior. The change in flexural stiffness from 1.5 to 1.0 mm was only −2.14%, which meets a reasonable convergence criterion of < 5%. The significant deviation observed at the 2.0 mm mesh size is likely due to an insufficient element distribution in critical stress concentration regions for that specific discretization level. Based on this analysis, a mesh size of 1.5 mm was selected for all subsequent simulations, as it provides a converged solution while maintaining computational efficiency. This observed sensitivity also highlights the computational complexity of the honeycomb geometry and justifies the use of a homogenized material model to make the extensive parametric study feasible.

4.3 | Validation of the Numerical Simulations

The precision of the finite element model was assessed by comparing the experimental and simulated slopes (P/y) of the initial linear elastic region of the load–displacement curves under three-point bending, as summarized in Table 5. The model successfully captured the qualitative trends of how geometric parameters influence flexural stiffness; however, quantitative discrepancies were observed, intensifying with shorter joint wall lengths and larger opening angles, with a maximum error of 21.52%.

These discrepancies are attributed to several inherent simplifications in the modeling approach. First, the homogenized model, while computationally efficient, oversimplifies the complex internal architecture of the 3D braided composite, ignoring effects of fiber orientation and the detailed yarn interlacing, particularly at critical stress-concentration regions like the "Y-shaped" junctions. Also, the possibility of local yarn compaction has not been addressed in the simplified model. Second, the assumption of isotropic, linear elastic material properties does not reflect the anisotropic nature and potential variability of the jute/epoxy composite. Third, the model relied on idealized interfacial and manufacturing assumptions, specifically frictionless contact conditions and the omission of process-induced imperfections such as geometric deviations and defects inherent to the VARTM process (e.g., local fiber nesting or yarn compaction).

To quantitatively validate the accuracy of the model, the Root Mean Square Error (RMSE) and the coefficient of determination (R^2) were calculated. The RMSE between the simulated values and the experimental means was 14.11 N/mm, and the R^2 value was 0.844. The high R^2 value demonstrates that the model reliably captures the stiffness trends caused by variations in geometric parameters, while the RMSE indicates the average level of deviation in the model's absolute value predictions.

It is explicitly acknowledged that the current homogenized model, while valuable for identifying parametric trends, cannot be considered fully confirmatory of the experimental data in a quantitative sense, particularly for structures with lower relative density. Methodological adjustments are necessary to improve quantitative fidelity. Future refinements should focus on: (1) implementing a more refined mesh in critical stress concentration regions; (2) incorporating anisotropic material properties derived from detailed characterization of the braided composite; and (3) accounting for both measured imperfections from manufactured samples and potential defects inherent to the VARTM process, such as local fiber nesting or yarn compaction.

Despite these quantitative discrepancies, the finite element model demonstrates a consistent ability to capture the correct influence trends of geometric parameters. Therefore, the model is deemed suitable for the primary objective of this study: conducting a comparative parametric analysis to identify key drivers of flexural performance in 3D braided composite honeycombs.

4.4 | Study on Parameters of Flexural Stiffness

Analysis of Formula (1) reveals that the slope of the displacement–load curve (P/y) reflects the flexural stiffness (D) of the 3D braided composite honeycombs, which is influenced by the material property (E), honeycomb thickness (H), cell joint wall length (l_2), cell free wall length (l_1), cell wall thickness (t/T), and cell opening angle (θ). The influence of these various factors on the flexural stiffness of 3D braided composite honeycombs is studied. The most common structure is a hexagonal honeycomb with an opening angle of 120°, with all variables referenced to model 120°-4.

4.4.1 | The Young's Modulus of Material

Except for the Young's modulus, the parameters of model 120°-4 were used and remained unchanged. The Young's modulus (E) varies from 4000 to 7000 MPa. As the Young's modulus of the material properties increases, the flexural stiffness of 3D braided composite honeycombs show a linear increase, as shown in Figure 7c. This is consistent with the conclusion obtained earlier through the analysis using Equation (1).

4.4.2 | The Height of Honeycomb

Except for the specimen thickness, all other parameters remain consistent with the 120°-4. The honeycomb thickness varies from 9 to 23 mm in increments of 2 mm. As the honeycomb thickness increases gradually, the flexural stiffness also increases and exhibits exponential growth, as shown in Figure 7d. This is also consistent with the conclusion obtained from the analysis using Equation (1): increasing the specimen thickness enhances the structural second moment of area, leading to exponential growth in flexural stiffness. However, this does not correspond to the exponent of 3 in Equation (1), the actual exponent is approximately 2.4, which is due to the influence of the honeycomb structure's shape.

4.4.3 | The Length of Joint Wall

All parameters, except for the joint wall length (l_2), are in line with the 120°-4 specification. The joint wall length varies from 15 to 21 mm in 1 mm increments. Figure 7e illustrates the impact of joint wall length on flexural stiffness, indicating an overall trend of increasing stiffness with the extension of wall length. It is noteworthy that the flexural stiffness at a joint wall length of 16 mm is lower than that at 15 and 17 mm. This is attributed to the different lengths of the joint wall, which lead to varying contact positions between the supporting fixture and the specimen within the same span, thus altering the structural shape that bears the bending load within the span, as depicted in Figure 7a. As the joint wall length increases, the contact position shifts from the free wall (area B) to the intersection area of the free wall and the joint wall (the area between area A and area B), and then to the joint wall (area A). The flexural stiffness generally shows an upward trend, but it experiences a slight decrease as the contact position nears the intersection area of the free and joint walls.

4.4.4 | The Length of Free Wall

Except for the free wall length (l_1), all other parameters are kept consistent with 120°-4. The free wall length increases from 17 to 22 mm in increments of 1 mm. The influence of free wall length on flexural stiffness is shown in Figure 7f. It can be observed that as the free wall length increases, the flexural stiffness shows an overall decreasing trend. However, the flexural stiffness at a free wall length of 20 mm is smaller than that at a free wall length of 21 mm.

As the length of the free wall changes, the contact position between the specimen and the support fixture within the same span will also vary, as shown in Figure 7a. Similar observations regarding changes in the joint wall length are noted: as the length of the free wall increases, the overall flexural stiffness shows a downward trend, with the flexural stiffness of the sample slightly decrease as the contact position approaches the intersection area of the free and joint walls.

4.4.5 | The Thickness of Free Wall

Except for the free wall thickness (t), all other parameters are consistent with the configuration of 120°-4. As the free wall thickness increases from 5 to 8 mm in increments of 0.5 mm, the influence of free wall thickness on flexural stiffness is depicted in Figure 7g. It is observed that as the free wall thickness

increases, the flexural stiffness gradually enhances, indicating an increased ability of the 3D braided composite honeycomb to resist flexural deformation.

According to Equation (1), an increase in free wall thickness corresponds to an increase in the Second moment of area of both the free wall and the joint wall cross-sections. Flexural stiffness is directly proportional to the Second moment of area of the cross-section. Therefore, the flexural stiffness of the 3D braided composite honeycomb exhibits an approximately linear growth with the increment of the free wall thickness.

When the wall thickness of the free wall is between 5 mm and 6 mm, the contact position between the supporting fixture and the sample is in the free wall. For wall thicknesses of 6.5 and 7 mm, the contact position is in the intersection area of the free and joint walls. When the wall thickness is 7.5 and 8 mm, the contact position is in the area of the joint wall.

It can be concluded that as the wall thickness of the free wall increases, the overall flexural stiffness shows an upward trend. However, the impact on flexural stiffness is greater when the contact position is on the joint wall.

4.4.6 | The Opening Angle

Except for the opening angle (θ), all other parameters are kept consistent with the 120°-4. The opening angle increases from 40° to 140°, and its effect on flexural stiffness is shown in Figure 7h. It can be observed that as the opening angle increases, the flexural stiffness gradually decreases. This is consistent with the experimental findings that flexural stiffness follows the order 60°-4 > 90°-4 > 120°-4. As the opening angle increases sequentially, according to Figure 4d, it is evident that the force F_y resisting flexural at the free end decreases progressively. Consequently, the specimen's ability to resist flexural deformation decreases accordingly, resulting in a gradual reduction in flexural stiffness.

4.4.7 | Stress Analysis

It can be observed that under 3-point flexural load, stress mainly concentrates at the intersection of the joint wall and the free wall. As stress increases, a tilted stress region forms on the free wall.

Taking the example of the 120°-4 specimen for analysis, the stress variations under different displacements are shown in Figure 8a. It is evident that stress first appears on the free wall, and with increasing displacement, stress gradually concentrates more at the intersection of the free wall and the joint wall, growing larger. During this process, shear stresses develop, extending toward the free wall. As indicated in Figure 8b, the positions of stress concentration and the regions of high stress on the free wall correspond to the locations and modes of fracture of the specimen. Figure 8c shows that the maximum strain area observed with 3D-DIC corresponds to the stress concentration positions identified by finite element analysis.

While a quantitative, point-to-point comparison of the full-field DIC and FEA strain values was not performed, the strong qualitative agreement in the location and pattern of the maximum strain zones provides confidence in the model's predictive capability for failure initiation. A more rigorous quantitative validation of strain fields will be a focus of future studies.

5 | Conclusion

This study experimentally and numerically investigated the effect of geometric parameters on the flexural performance of 3D braided composite honeycombs. The main conclusions are as follows:

1. The flexural performance is highly sensitive to geometric parameters. For 90° honeycombs, decreasing the joint wall length from 55 to 4 mm reduces the maximum load by ~26% and the flexural stiffness (P/y) by ~55%, while increasing maximum deflection by ~61%. For a 17 mm joint wall, increasing the opening angle from 60° to 120° decreases the maximum load by ~32% and the flexural stiffness by ~55%.
2. The 3D braided composite honeycombs consistently exhibited sudden brittle fracture. Failure consistently initiates at the stress-concentrated "Y-shaped" junction, leading to an inclined shear-type fracture on the free wall. This identifies the junction as the critical region requiring reinforcement in design.
3. A homogenized finite element model effectively predicted the trends in flexural stiffness. To maximize flexural stiffness, the optimal design strategy involves employing a smaller opening angle combined with a shorter joint wall, while ensuring that the support fixture contacts the joint wall directly rather than the intersection region. To enhance energy absorption or deflection capacity, a larger opening angle paired with a longer joint wall is recommended. Flexural stiffness demonstrates a linear relationship with wall thickness and an exponential relationship with specimen height (exponent ~2.4), providing efficient and strategic pathways for performance enhancement in structural design.
4. The strong correlation between DIC-measured strain concentrations, FEA-predicted stress fields, and actual fracture locations validates the failure mechanism and provides confidence in the model for guiding design.

These findings have the potential to inform future research and development in composite honeycomb, particularly in applications where bending resistance and structural integrity are critical, such as in sandwich panels for transportation and aerospace industries, laying a foundation for subsequent optimization studies.

This work has limitations, including the homogenized model's simplification of the complex architecture, leading to

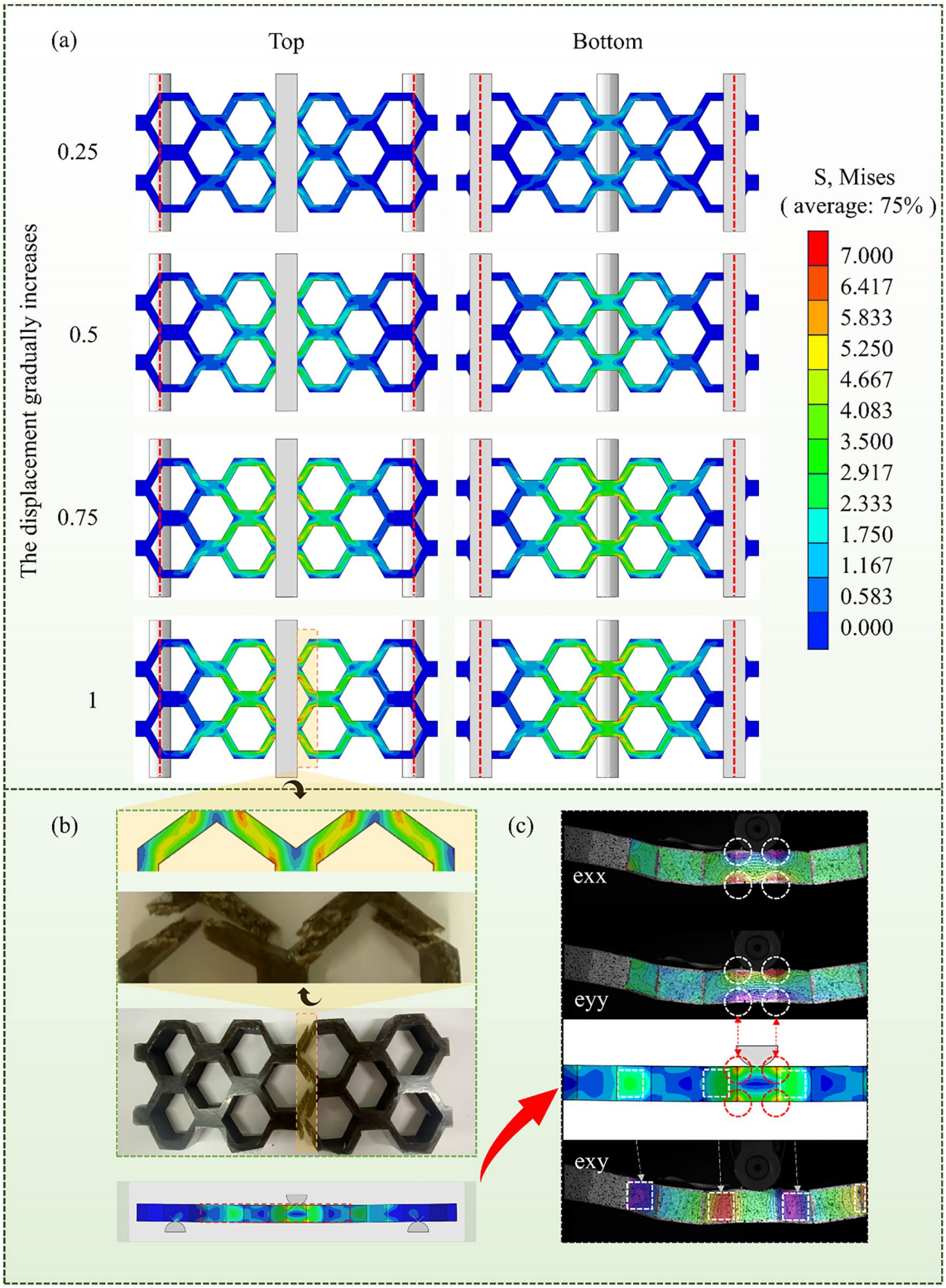

FIGURE 8 | The analysis of stress, strain and damage location: (a) stress variation of FEA (b) correlation between FEA stress distribution and fracture location of the specimen (c) correlation between 3D-DIC strain distribution and FEA stress distribution.

quantitative discrepancies and the focus on linear elastic behavior prior to failure. Future work should involve detailed microstructural analysis, investigation of dynamic/fatigue loading and environmental effects, and development of multi-scale models capable of predicting progressive damage.

Author Contributions

Qianqian Li: conceptualization, methodology, investigation, writing – original draft, writing – review and editing, visualization, and data

curation. **René Alderliesten:** writing – review and editing, supervision. **Honghua Zhang:** software. **Yan Zhang:** investigation. **Hui Zhang:** project administration and funding acquisition. **Wei Li:** supervision and resources. **Jianyong Yu:** supervision and resources. **Yasmine Mosleh:** writing – review and editing, supervision.

Acknowledgments

The authors gratefully acknowledge the China Scholarship Council (Grant No. 202106630029) for financial support. They also extend their appreciation to the technicians at the Department of Aerospace Structures and Materials, Delft University of Technology (TU Delft), for technical assistance. Additionally, this work was supported by the Open Project Program of the Shanghai High Performance Fiber and Composites Center (Province-Ministry Joint), Center for Civil Aviation Composites, Donghua University.

Funding

This work was supported by China Scholarship Council, 202106630029.

Conflicts of Interest

The authors declare no conflicts of interest.

Data Availability Statement

The authors have nothing to report.

References

1. J. Wang, B. Li, Y. Zhu, W. Liu, L. Wu, and Y. Lv, "Mechanical Modeling of Bending Stiffness Degradation for Soft-Honeycomb Sandwich Structure Under CW Laser Heating," *AIP Advances* 10, no. 2 (2020): 025201.

2. S. Song, C. Xiong, F. Tao, J. Yin, Y. Zhang, and S. Zhang, "Size Effect of Composite Kagome Honeycomb Sandwich Structure Reinforced With PMI Foams Under Quasi-Static Bending: Experiment Tests and Numerical Analysis," *Composite Structures* 296 (2022): 115832.

3. Y. Lin, C. Xiao, H. Li, X. Zhang, Y. Hou, and J. Tao, "Flexural and Low-Velocity Behavior of GFPP/DP980 Honeycomb Sandwich Structure Inspired by Fiber Metal Laminates," *Polymer Composites* 46 (2025): 5064–5080.

4. A. L. Amir, M. R. Ishak, N. Yidris, M. Y. M. Zuhri, M. R. M. Asyraf, and S. Z. S. Zakaria, "Influence of Woven Glass-Fibre Prepreg Orientation on the Flexural Properties of a Sustainable Composite Honeycomb Sandwich Panel for Structural Applications," *Materials* 16, no. 14 (2023): 5021.

5. A. Akatay, M. Ö. Bora, S. Fidan, and O. Çoban, "Damage Characterization of Three Point Bended Honeycomb Sandwich Structures Under Different Temperatures With Cone Beam Computed Tomography Technique," *Polymer Composites* 39, no. 1 (2015): 46–54.

6. S. Prabhakaran, V. Krishnaraj, K. Shankar, M. Senthilkumar, and R. Zitoune, "Experimental Investigation on Impact, Sound, and Vibration Response of Natural-Based Composite Sandwich Made of Flax and Agglomerated Cork," *Journal of Composite Materials* 54, no. 5 (2019): 669–680.

7. Z. Song, L. Su, M. Yuan, S. Shang, and S. Cui, "Self-Cleaning, Energy-Saving Aerogel Composites Possessed Sandwich Structure: Improving Indoor Comfort With Excellent Thermal Insulation and Acoustic Performance," *Energy and Buildings* 310 (2024): 114098.

8. Z. Li, Y. Zhou, X. Kong, et al., "Sound Absorption Performance of a Micro-Perforated Plate Sandwich Structure Based on Selective Laser Melting," *Virtual and Physical Prototyping* 19, no. 1 (2024): e2321607.

9. A. Haris and H. P. Lee, "Sound Transmission Loss and Compression Properties of Sandwich Panels With Milli-Perforated Honeycomb Core," *Fibers and Polymers* 23, no. 11 (2022): 3138–3145.

10. G.-C. Yu, L.-J. Feng, and L.-Z. Wu, "Thermal and Mechanical Properties of a Multifunctional Composite Square Honeycomb Sandwich Structure," *Materials & Design* 102 (2016): 238–246.

11. M. Nie, Y. Ren, H. Wang, et al., "Recovery of Wave-Absorbing Efficiency for Honeycomb Sandwich Structure Under Penetrating Damage via Composite Patch Electromagnetic Parameters Design," *Materials Today Communications* 41, no. 1 (2024): 110799.

12. R. Huang, L. Cheng, Z. Ji, et al., "Simultaneous Enhancement Design of Polymethacrylimide Foam Sandwich Structure With EM Wave Transmission and Compressive Properties," *Aerospace Science and Technology* 155, no. 2 (2024): 109656.

13. E. Bahmanpour, A. Montazeri, A. Saeedi, and M. Mahnama, "Flexural Behaviors of Asymmetric re-Entrant Auxetic Honeycombs," *European Journal of Mechanics – A/Solids* 109 (2025): 105475.

14. J. R. Dutra, S. L. Moni Ribeiro Filho, A. L. Christoforo, T. H. Panzera, and F. Scarpa, "Investigations on Sustainable Honeycomb Sandwich Panels Containing Eucalyptus Sawdust, Piassava and Cement Particles," *Thin-Walled Structures* 143 (2019): 106191.

15. A. Stocchi, L. Colabella, A. Cisilino, and V. Álvarez, "Manufacturing and Testing of a Sandwich Panel Honeycomb Core Reinforced With Natural-Fiber Fabrics," *Materials & Design* 55 (2014): 394–403.

16. L. Pehlivan and C. Baykasoğlu, "An Experimental Study on the Compressive Response of CFRP Honeycombs With Various Cell Configurations," *Composites Part B: Engineering* 162 (2019): 653–661.

17. X. Wang, X.-L. Shi, Q.-K. Meng, Y.-c. Hu, and L.-h. Wang, "Bending Behaviors of Three Grid Sandwich Structures With Wood Facing and Jute Fabrics/Epoxy Composites Cores," *Composite Structures* 252 (2020): 112666.

18. J. Yan, K. Liu, H. Zhou, Z. Zhang, B. Gu, and B. Sun, "The Bending Fatigue Comparison Between 3D Braided Rectangular Composites and T-Beam Composites," *Fibers and Polymers* 16, no. 3 (2015): 634–639.

19. A. P. Mouritz, M. K. Bannister, P. J. Falzon, et al., "Review of Applications for Advanced Three-Dimensional Fibre Textile Composites," *Composites Part A: Applied Science and Manufacturing* 30, no. 12 (1999): 1445–1461.

20. Q. Q. Li, H. H. Zhang, Y. Mosleh, et al., "Development and Analysis of a Three-Dimensional Braided Honeycomb Structure," *Textile Research Journal* 93, no. 9 (2023): 2078–2094.

21. Q. Q. Li, Y. Mosleh, R. C. Alderliesten, et al., "Effects of Different Joint Wall Lengths on In-Plane Compression Properties of 3D Braided Jute/Epoxy Composite Honeycombs," *Journal of Reinforced Plastics and Composites* 43, no. 9–10 (2024): 547–564.

22. I. C. Sukmaji, W. R. Wijang, S. Andri, et al., "Application of Sandwich Honeycomb Carbon/Glass Fiber-Honeycomb Composite in the Floor Component of Electric Car," 2017, https://doi.org/10.1063/1.4968309.

23. D. H. Chen, "Bending Deformation of Honeycomb Consisting of Regular Hexagonal Cells," *Composite Structures* 93, no. 2 (2011): 736–746.

24. A. Cernescu, J. Romanoff, H. Remes, N. Faur, and J. Jelovica, "Equivalent Mechanical Properties for Cylindrical Cell Honeycomb Core Structure," *Composite Structures* 108 (2014): 866–875.

25. M. F. He and W. B. Hu, "A Study on Composite Honeycomb Sandwich Panel Structure," *Materials & Design* 29, no. 3 (2008): 709–713.

26. L. Tripathi and B. K. Behera, "Flatwise Compression Behavior of 3D Woven Honeycomb Composites," *Journal of Industrial Textiles* 52 (2022): 1–24.

27. L. Tripathi and B. K. Behera, "Influence of Different Structural Parameters of 3D Woven Honeycomb Composites on Three-Point Bending Behavior," *Journal of the Textile Institute* 115, no. 6 (2023): 877–892.

28. J. Y. Chen, H. Fang, W. Q. Liu, et al., "Energy Absorption of Foam-Filled Multi-Cell Composite Panels Under Quasi-Static Compression," *Composites Part B: Engineering* 153 (2018): 295–305.

29. M. Fu and J. Yin, "Equivalent Elastic Parameters of the Honeycomb Core," *Acta Mechanica Sinica* 31, no. 1 (1999): 113–118.

30. L. Y. Zhou, M. C. Wu, and H. Z. He, "Research of Plastic Honeycomb Sandwich Plates' Bending Stiffness by Finite Element Method," *Plastics* 45, no. 3 (2016): 78–80.

31. Q. Q. Li, Y. Mosleh, R. C. Alderliesten, et al., "In-Plane Compressive Properties of 3D Braided Jute/Epoxy Composite Honeycombs: Structure-Property Relationships," *Journal of Reinforced Plastics and Composites* (2025): 1–9.

32. Y. Y. Zhang, H. M. Li, Y. H. Gao, et al.,"Multi-Scale Modeling and Elastic Properties Prediction of 3D Four-Directional Tubular Braided Composites," *Composite Structures* 292 (2022): 115632.

Supporting Information

Additional supporting information can be found online in the Supporting Information section. **Data S1:** Supporting Information.